1. **Manuscript Title**

Neuropeptides with different cellular targets elicit similar output in a central pattern generating circuit

2. **Abbreviated Title**

Different neuropeptides elicit similar circuit output

3. **Author Names and Affiliations**

Elizabeth M. Cronin
Anna C. Schneider
Farzan Nadim
Dirk Bucher

Federated Department of Biological Sciences, New Jersey Institute of Technology and Rutgers University, Newark, NJ 07102

4. **Author Contributions**

EMC, FN, and DB designed research; EMC performed research; EMC, ACS, and DB analyzed the data; EMC, DB, and FN wrote the paper.

5. **Correspondence should be addressed to**

Dirk Bucher
bucher@njit.edu

6. **Number of Figures: 8**

7. **Number of Tables: 1**

8. **Number of Multimedia: 0**

9. **Number of words for Abstract: 246**

10. **Number of words for Introduction: 684**

11. **Number of words for Discussion: 1379**

12. **Acknowledgements**

We thank Gareth Russell for advice on statistics, and Omar Itani, Jorge Golowasch, and Dawn Blitz for helpful suggestions and comments.

13. **Conflict of Interest**

The authors report no conflict of interest.

14. **Funding sources**

NIH MH060605 to FN and DB, DFG SCHN 1594/1-1 to ACS

Abstract

Neuromodulation lends flexibility to neural circuit operation. However, the general notion that different neuromodulators sculpt neural circuit output into distinct and characteristic patterns is complicated by interindividual variability. In addition, some neuromodulators converge onto the same signaling pathways, with similar effects on neurons and synapses. We compared the effects of three neuropeptides on the rhythmic pyloric circuit in the crab *Cancer borealis* stomatogastric nervous system. Proctolin (PROC), crustacean cardioactive peptide (CCAP), and red pigment concentrating hormone (RPCH) all activate the same modulatory inward current, I_{MI}, and have convergent actions on synapses. However, while PROC targets all four neuron types in the core pyloric circuit, CCAP and RPCH target the same subset of only two neurons. After removal of spontaneous neuromodulator release, none of the neuropeptides restored the control cycle frequency, but all restored the relative timing between neuron types. Consequently, differences between neuropeptide effects were mainly found in the spiking activity of different neuron types. We performed statistical comparisons using the Euclidean distance in the multidimensional space of normalized output attributes to obtain a single measure of difference between modulatory states. Across preparations, circuit output in PROC was distinguishable from CCAP and RPCH, but CCAP and RPCH were not. However, we argue that even between PROC and the other two neuropeptides, population data overlapped enough to prevent reliable identification of individual output patterns as characteristic for a specific neuropeptide. We confirm this notion by showing that blind classifications by machine learning algorithms are only moderately successful.

Introduction

The flexibility of neural circuit operation that allows adaptation of activity patterns to different behavioral contexts is largely owed to neuromodulation (Doi and Ramirez, 2008; Marder, 2012; Bucher and Marder, 2013; Nadim and Bucher, 2014; Diaz-Rios et al., 2017; McCormick et al., 2020). Consequently, specific types of circuit activity, and even entire brain states, have been associated with specific neuromodulators. The underlying assumption is that a given neuromodulator (or combination of multiple neuromodulators) elicits a characteristic activity pattern that is distinguishable from those elicited by other neuromodulators. This assumption may be relatively straightforward to validate in cases where different neuromodulators are associated with qualitatively different behaviors or brain states. For example, switching between crawling and swimming gaits in *C. elegans* is associated with differential influences of dopamine and serotonin (Vidal-Gadea et al., 2011), and sleep-wake cycles in mammals are controlled by differential actions of multiple neuromodulators (Jones, 2020). It may be less straightforward in cases where neuromodulators push circuits across a continuous spectrum of activity attributes, without clear transitions that correspond to the selection of distinct behaviors. For example, circuits controlling locomotion can execute the same gait at different speeds and strengths (Grillner, 2006; Mullins et al., 2011; Zhang et al., 2014; Le Gal et al., 2017). In addition, the question of what constitutes circuit activity characteristic for a specific modulatory state is complicated by convergent actions of different neuromodulators, and by interindividual variability.

Neuromodulators, principally biogenic amines and neuropeptides, act mostly through G-protein-coupled receptors and alter intrinsic neuronal excitability and synaptic function, typically in a cell type-specific manner. As their release is often paracrine or hormonal, they affect multiple or all circuit neurons at once, and the way they sculpt circuit activity depends on patterns of convergence and divergence in their cellular and subcellular actions (McCormick and Williamson, 1989; Harris-Warrick and Johnson, 2010; Harris-Warrick, 2011; Bucher and Marder, 2013; Nadim and Bucher, 2014; Due et al., 2022). Two neuromodulators can target distinct subsets of circuit neurons, but in neurons that express receptors to both, their effects on ion channels or synaptic release can be either divergent or convergent. If receptor activation converges on the same signaling pathway and subcellular targets in enough circuit neurons, circuit effects of both neuromodulators may be similar and only differ depending on how, when, and in which quantities they are released (McCormick and Williamson, 1989).

Another confounding factor for consistent and characteristic neuromodulator effects is interindividual variability. Ionic currents and synapses targeted by neuromodulation can vary substantially across individuals, and circuit outputs under the same conditions can show some degree of variability (Marder and Goaillard, 2006; Marder et al., 2007; Calabrese et al., 2011; Golowasch, 2014; Marder et al., 2014b; Goaillard and Marder, 2021). Neuromodulator receptor expression

and modulatory effects on individual neurons or synapses can also be quite variable (Garcia et al., 2015; Maloney, 2021), and neuromodulation can either promote or counteract interindividual variability (Hamood and Marder, 2014; Marder et al., 2014a; Maloney, 2021; Xu et al., 2021; Schneider et al., 2022; Tamvacakis et al., 2022).

Here we ask to which degree different neuromodulators with convergent cellular actions but divergent circuit targets produce reliably distinguishable circuit activity across individuals. We compare the circuit outputs of the pyloric central pattern generator of the crustacean stomatogastric ganglion (STG)(Marder and Bucher, 2007; Stein, 2009; Daur et al., 2016) across bath applications of different neuropeptide modulators. While in this system modulatory effects are tractable from cellular actions to circuit activity, surprisingly few attempts have been made to directly compare the actions of different neuromodulators on circuit output (Marder and Weimann, 1992). The principal action of these neuropeptides is the activation of a voltage-gated inward current, I_{MI} (Golowasch and Marder, 1992; Swensen and Marder, 2000; Gray and Golowasch, 2016; Gray et al., 2017). Despite this convergence, different neuropeptides are thought to produce distinct circuit outputs because each targets an overlapping but different subset of circuit neurons (Swensen and Marder, 2001). However, we show here that across a population of individuals with varying neuromodulator responses, even statistically distinguishable output patterns are not sufficiently characteristic to allow identification of neuromodulatory state from individual recordings.

Materials and Methods

Experimental preparation

All experiments were performed on adult male crabs (*Cancer borealis*) obtained from local fish markets and maintained in recirculating artificial seawater tanks at 12°C until use. Crabs were anesthetized in ice for ~30 minutes prior to dissection. Dissections were performed in saline containing: 11 mM KCl, 440 mM NaCl, 13 mM $CaCl_2 \cdot 2H_2O$, 26 mM $MgCl_2 \cdot 6H_2O$, 11.2 mM Tris base, 5.1 mM maleic acid, with a pH of 7.4. The stomatogastric nervous system (STNS), including the stomatogastric ganglion (STG), esophageal ganglion (OG), the pair of commissural ganglia (CoG), and the motor nerves (schematic in Figure 1A) were dissected from the stomach and pinned to a saline-filled, Sylgard-coated (Dow Corning) Petri dish. The STG was desheathed to facilitate intracellular impalement of neuronal somata and allow for easy permeation of bath-applied neuromodulators. Preparations were superfused with chilled (11-13°C) physiological saline using a peristaltic pump (Dynamax).

Electrophysiological recordings

In this study we focus on the core subcircuit of the pyloric circuit which consists of 4 neuron types that have a well-characterized connectivity pattern (Fig. 1B). The two pyloric dilator (PD) neurons are motor neurons that are electrically coupled to each other and to the anterior burster (AB) neuron. The PD and AB neurons form the pacemaker kernel of the pyloric CPG. The follower neurons, including the single lateral pyloric (LP) neuron and the 3-5 pyloric (PY) constrictor neurons, sequentially burst in rebound from inhibition by the pacemakers. The pyloric rhythm is therefore a triphasic bursting pattern (Marder and Bucher, 2007) (Fig. 1B). The activity of the PD, LP, and PY neurons was recorded simultaneously with multiple intracellular soma recordings and extracellular motor nerve recordings.

Extracellular recordings from identified motor nerves were obtained with pairs of stainless-steel wire electrodes, placed inside and outside of petroleum jelly wells built to electrically isolate small sections of nerve. Extracellular signals were amplified using differential AC amplifiers (A-M Systems, model 1700). PD activity was recorded from the pyloric dilator nerve (pdn). LP activity was recorded from the lateral ventricular nerve (lvn), where LP contributes the signal with the largest amplitude. PY activity was recorded from the pyloric constrictor nerve (pyn). Intracellular recordings were obtained from neuronal somata in the STG using sharp glass microelectrodes prepared with the Flaming-Brown micropipette puller (P97, Sutter Instruments). They were filled with an electrolyte solution of 0.6 M K_2SO_4 and 20 mM KCl, yielding tip resistances of 20-30 MΩ. Electrodes were positioned with MicroStar motorized manipulators (Scientifica). Intracellular signals were amplified with Axoclamp 2B and 900A amplifiers (Molecular Devices). Neurons were identified by their characteristic waveforms and by matching their spike patterns to the extracellular activities recorded in the corresponding motor nerves. Both intracellular and extracellular signals were digitized at 10 kHz using a Micro1401 digitizer with its accompanying Spike2 data acquisition software (Cambridge Electronic Design).

Neuromodulator application

In all preparations, petroleum jelly wells were built around the STG for focal neuromodulator superfusion. In addition, a well was built around the stomatogastric nerve (stn), the sole input nerve to the STG from other central nervous system ganglia. The triphasic pyloric rhythm was recorded first with intact descending modulatory inputs from the CoGs and OG to the STG. Subsequently, the STG was decentralized, i.e., modulatory inputs were removed by blocking action potential conduction in descending axons. This was achieved by application of 100 nM TTX (tetrodotoxin citrate, Biotium) in a 750 mM sucrose (Sigma) solution to the well around the stn. Neuromodulators were then applied to the STG at a concentration of 1 µM for at least 5 min. When multiple modulators were applied sequentially to the same preparation, each modulator was washed out for at least 30 min. These modulators included DA (dopamine: 3-hydroxytyramine hydrochloride, Sigma) and the neuropeptides PROC (proctolin, custom synthesis by RS synthesis), CCAP (crustacean cardioactive peptide, Bachem), and RPCH (red pigment concentrating hormone, Bachem). DA stock solutions of 1 mM in distilled water were always made fresh and kept in the dark on ice for no longer than 1 h. PROC and CCAP were initially dissolved in distilled water, and RPCH in dimethyl sulfoxide (DMSO, Sigma), to yield stock solutions of 1 mM, which were then aliquoted and held at -20°C until needed. Final dilution of modulators to the experimental concentration occurred immediately before application in chilled saline.

Initial pattern analysis

Initial analysis of circuit activity patterns was performed using custom-written scripts in Spike2. Cycle-to-cycle spike and burst detection allowed extraction of several output pattern attributes (Fig. 1B). Cycle period (*P*) was defined as the latency between consecutive PD burst starts. Cycle frequency (F_{cycle}) was then calculated as 1/*P*. Using the PD burst start as the reference time, we measured the latencies of all burst starts (on) and burst ends (off), and burst durations as the time between burst starts and burst ends. Latencies were then divided by *P* to yield values for phase (φ). The numbers of spikes per burst (*#spks*) were determined for all neurons, and the spike frequencies within bursts (F_{spk}) were calculated as *#spks*-1 divided by the burst duration. From each individual recording and state, we used a minimum of 20 cycles and determined the mean value for each attribute.

While all output attributes are potentially interdependent, some are unambiguously redundant. Therefore, we only used a subset of attributes for our analyses. *P* and F_{cycle} are the inverse of each other, so we only used F_{cycle}. As latencies and burst durations were strongly dependent on *P*, we only used the relative timing (φ_{on} and φ_{off}). We also excluded duty cycle (burst duration/*P*), as it is merely the difference between φ_{off} and φ_{on}. F_{spk} and *#spks* are obviously interdependent. However, they were not strongly correlated in at least a subset of neurons and conditions (e.g., LP and PY in neuropeptides showing R^2 values < 0.5). Therefore, we used both.

In extracellular recordings, spikes from the two PD axons in the pdn and from multiple PY axons in the pyn summate, which renders individual spike detection ambiguous. Therefore, all analyses that included the full set of rhythm attributes were performed only from experiments in which we established simultaneous intracellular recordings from PD, LP and PY neurons. Extracellular recordings were only used for additional analyses of burst timing, as indicated in the Results section. Basic descriptive statistics of pattern attributes and comparisons across modulator treatments with analysis of variance (ANOVA) and subsequent Holm-Sidak *post-hoc* tests were performed using SigmaPlot (version 12.0, Systat Software). All subsequent data handling and analysis described in the following was performed in MATLAB (version 2022a, Mathworks). Statistical significance was assumed at $p < 0.05$ and is indicated as * $p < 0.05$, ** $p < 0.01$, and *** $p < 0.001$.

Euclidean distance and multivariate permutation tests

For comparisons between modulatory conditions in multiple dimensions, we determined the mean of each attribute across experiments and calculated the Euclidean distance:

$$\Delta(A,B) = \sqrt{(a_1 - b_1)^2 + (a_2 - b_2)^2 + \ldots + (a_k - b_k)^2},$$

where *A* and *B* are two modulatory conditions, and a_1 to a_k and b_1 to b_k are the means of the different output pattern attributes as Cartesian coordinates in k-dimensional Euclidean space.

We did this first with attributes of the same units across different neurons: $\Delta\varphi$ as the distance in 5 dimensions (φPD_{off}, φLP_{on}, φLP_{off}, φPY_{on}, φPY_{off}), Δ*#spks* in 3 dimensions (PD *#spks*, LP *#spks*, PY *#spks*), and ΔF_{spk} in 3 dimensions (PD F_{spk}, LP F_{spk}, PY F_{spk}). To be able to include attributes of different units in the same analysis, we standardized each attribute by calculating *z*-scores:

$$z = \frac{x - \bar{x}}{SD},$$

where *x* is an attribute in a single experiment, and $\bar{x}$ and *SD* are, respectively, the mean and standard deviation of that attribute across all experiments and modulatory states. Once all attributes were z-scored, we calculated the Euclidean distance between pairs of conditions in 12 dimensions (F_{cycle}, 5 dimensions of φ, 3 dimensions of *#spks*, 3 dimensions of F_{spk}). Principal component analysis (PCA) was used to visualize the 12-dimensional data in the three-dimensional space of the first three principal components.

To determine if differences between two modulatory states were statistically significant, we used a modified version of the multi-variate permutation test (Anderson, 2001; Nichols and Holmes, 2002). For example, to compare data from modulatory states *A* and *B* with respective sample sizes n*A* and n*B* (each sample with k coordinates), we first calculated the Euclidean distance between the means of the two modulatory states, as described above. The data from the two groups were then pooled into a single group, and data points were randomly reassigned into two new groups, *A*i and *B*i, of the same respective sizes (n*A* and n*B*) by exchanging (permuting) elements between the two groups. We then calculated the Euclidean distance between the means of the two new groups *A*i and *B*i. This process was repeated for 9999 permutations of *A*i and *B*i, and the one-sided p-value of the test was calculated as the proportion of permutations for which the Euclidean distances were larger than the original distance of A and B. The determination of statistical significance was made with an alpha level of 0.05.

Machine learning analysis

As an independent test for how well output patterns from different modulatory conditions can be distinguished, we used supervised machine learning (ML) algorithms. Pattern recognition and time series classification networks were created using the Deep Learning Toolbox (version 14.2) and the Parallel Computing Toolbox (version 7.4) in MATLAB.

Because training outcome partially depends on initial values of ML network parameters and our datasets were relatively small for this purpose, we used a bootstrapping approach to sample the distribution of classification accuracy based on network initialization and dataset splitting in training and test data. For each modulatory condition, we split the corresponding dataset randomly into 70% training data and 30% test data. We then randomly initialized 50 ML networks, trained them, and kept the most accurate one. On the next run, we again split the dataset randomly into training and test data and repeated the same process. We repeated this process for 100 runs, which resulted in 100 networks of varying accuracy. We then classified the test data with the corresponding networks and calculated the percentage of correct and false positive classifications across these 100 ML networks for each modulatory condition.

We first tested this approach with the *z*-scored attributes that we had extracted for our Euclidean distance analysis. Because all temporal features of output activity are explicit (already quantified) in these attributes, we could employ a shallow feedforward pattern recognition network (Janiesch et al., 2021). This ML algorithm was created with the default settings of the MATLAB function “patternnet” and consisted of one input layer, one hidden layer with 50 units, and one output layer.

We also performed a different ML analysis based only on (not *z*-scored) spike times and F_{cycle}. For this, we extracted spike times of the three neurons (PD, LP, and PY) from 30 s of recording data from each trial in each experiment and sorted them into a fixed number of bins per cycle, thereby generating spike phase histograms. To account for differences in F_{cycle} across modulatory states, we optionally biased the bin counts by adding the *z*-scored values of F_{cycle}. The more minimally processed data does not explicitly contain relative timing information and therefore requires an ML network that is able to process temporal sequences within and across neurons. Therefore, we resorted to using a time series classification network (Goodfellow et al., 2016). This recurrent neural network consisted of a sequence input layer

with three channels (one for each neuron), a bi-directional long short-term memory layer (LSTM, Schuster and Paliwal (1997)) with 50 hidden units set to output the last time step of the sequence, a fully connected layer with five channels (one for each modulatory state), a softmax layer to convert real numbers into probability distributions, and the classification layer. We empirically determined that in order to obtain trained networks with satisfactory accuracy, we had to change the default settings in MATLAB to use the Adam optimizer with a denominator offset of 10^{-6}, set the mini-batch size to accommodate all input data in one batch, allow a maximum of 1000 epochs for training, validate the network at every other iteration with the test data, and set the patience of validation stopping to 25. It would have been possible to use the original voltage traces for time series classification with this network (Janiesch et al., 2021), but the minimal processing reduced the amount of data sufficiently to train the network on a desktop PC in a reasonable amount of time.

To visualize the classification results from the ML networks, we show classification matrices modified from the commonly used confusion matrices to account for the unequal numbers of recordings from each modulatory state. The matrices show the actual modulatory state as the true class for each row, and the percentage of correct and incorrect classifications in each column for that row. Therefore, percentages add up to 100% in each row instead of for the whole matrix.

Results

Circuit outputs in different neuropeptides were distinguishable by spiking behavior but not burst timing.

We characterized the pyloric rhythm by determining output pattern attributes from simultaneous recordings of PD, LP, and PY neurons (Fig. 1B). Intracellular recordings showed slow wave oscillations and attenuated spikes typical for soma recordings of STG neurons, with the well-characterized triphasic sequence between neurons (Marder and Bucher, 2007). We measured attributes across different modulatory states, with intact descending input, after decentralization, and after application of neuropeptides (Fig. 2A). We assumed that with intact descending modulatory inputs, all neurons and synapses were modulated, while decentralization removed all modulatory control of intrinsic and synaptic properties. PROC application activates I_{MI} in AB, PD, LP, and ~70% of PY neurons, while both CCAP and RPCH activate I_{MI} only in AB and LP (Swensen and Marder, 2001). Both PROC and CCAP enhance synaptic currents in the reciprocal connections between the pacemaker neurons and LP (Li et al., 2018), and RPCH enhances the LP to pacemaker synaptic current (Atamturktur and Nadim, 2011), but effects on the pacemaker to PY and PY to LP synapses have not been studied.

We first used the measured output pattern attributes for standard statistical evaluation (Fig. 2B-E). In most cases, the required long washes between neuropeptide applications prevented us from obtaining data from all modulatory states in the same experiment. Therefore, all statistics were performed as unpaired comparisons. Decentralization substantially slowed the pyloric rhythm and none of the neuropeptides on their own recovered F_{cycle} to the intact value (Fig. 2B). In fact, only in RPCH was F_{cycle} significantly increased from the decentralized state. F_{cycle} in RPCH was also larger than in CCAP, but not distinguishable from PROC. The activity phases of the three neurons were changed substantially by decentralization, but all neuropeptides essentially restored the phase relationships to the intact state (Fig. 2C). Only φLP_{on} in CCAP was different from the intact pattern. In contrast, the three neuropeptides had several differential effects on *#spks* and F_{spk} (Fig. 2D, E). LP *#spks* differed between PROC and CCAP and between CCAP and RPCH. PY *#spks* in PROC differed from both CCAP and RPCH. PD F_{spk} differed between all peptides, and PY F_{spk} between PROC and CCAP. It therefore appears that, at least at first pass, the modulated states should be more easily distinguishable based on spiking activity within bursts than based on F_{cycle} or phase relationships.

Covariance showed interdependence of circuit output attributes.

The type of analysis shown in Figure 2 comes with some caveats. In recurrent circuits, all activity attributes within and across different neuron types potentially depend on each other. To establish an effect of a neuromodulator, it is appropriate to ask whether the modulator changes a given single attribute like F_{cycle} or *#spks* in a specific neuron. However, when many attributes are separately tested across two or more circuit states, and in several neurons, the

interdependence of these attributes is at least partially ignored. Statistical tests like ANOVA may report the presence of such interdependence but can only be used for attributes within the same category (e.g., all activity phases).

Such interdependence is illustrated by the relationships between *P* (or equivalently, F_{cycle}) and burst timing. In the intact pyloric circuit, latencies of burst on and off times scale with *P*, so that values of φ are largely independent of F_{cycle}. This is true both within individuals when F_{cycle} is experimentally altered (Hooper, 1997; Tang et al., 2012; Soofi et al., 2014), and across individuals that differ in F_{cycle} under control conditions (Bucher et al., 2005; Goaillard et al., 2009; Anwar et al., 2022). We found that phases are also largely independent of frequencies across different modulated states. In pooled data from all modulated conditions (intact, PROC, CCAP, RPCH), latencies scaled roughly proportionally with *P* across all states (Fig. 3A, top left panel). Linear regressions showed small offsets and large R^2 values (Table 1). Consequently, values of φ were mostly independent of F_{cycle} (Fig. 3A, top right panel). In contrast, latencies did not scale proportionally with *P* in decentralized preparations, rendering φ values dependent on F_{cycle}. (Fig. 3A, bottom panels) The only exception was PY_{off}, as PY neurons usually burst until the end of each cycle when they are inhibited by the next pacemaker burst (φPY_{off} is always close to 1).

We also analyzed the relationship between *P* or F_{cycle} and spiking activity (Fig. 3B, C and Table 1). Across all states, values of *#spks* change with *P* in all neurons (Fig. 3B). However, this scaling was not proportional, and coefficients of determination were small. F_{spk} across all states was also dependent on F_{cycle} in all neurons (Fig. 3C), and F_{spk} in LP and PY scaled proportionately with F_{cycle}. In this case, R^2 values were larger than for the relationship between *#spks* and *P*, but smaller than for the relationship of latencies and *P*.

These results suggest that the constant phases across $\underline{F}_{cycle}$ arise from a stable dependence of latency on *P* that is independent of which neuropeptide is present, while spiking behavior within bursts is more malleable.

Multidimensional comparison confirmed the similarity of phase relationships in different modulated conditions.

In addition to interdependence of attributes, quantification of differences is usually only established one-by-one for each attribute. For our analysis, however, we wanted to ask how different or similar the entire output patterns are across different modulatory states, preferably with a method that yields a single measure of difference between each pair of modulatory states. To this end, we measured the distance between circuit outputs in the multidimensional attribute space. As proof-of-concept, we first did this type of analysis separately for attributes with the same units.

We first examined the effects of the modulators in the five-dimensional φ space. For ease of visualization, we plotted two different combinations, each showing three of the five φ values (LP_{on}, LP_{off}, PY_{on} in Fig. 4A; PD_{off}, LP_{off}, PY_{off} in Fig. 4B). The distribution of data points from each individual experiment (Fig. 4Ai, Bi) showed substantial overlap between the modulated states (intact, PROC, CCAP, RPCH) but much smaller overlap between the decentralized state and all modulated states. To visualize the mean differences (Fig. 4Aii, Bii), we plotted the mean Cartesian coordinates (centroid) for each state as a sphere and connected each pair of centroids with a line representing the three-dimensional Euclidean distance. In both combinations of phases, the centroids of the modulated states clustered while the centroid of the decentralized state was more distant, resulting from differences in all dimensions but PY_{off}.

To combine all dimensions, we plotted the one-dimensional projections of the Euclidean distances in the five-dimensional φ space (Δφ) between all pairs of modulatory states (Fig. 4C), along with the results of statistical evaluation from multivariate permutation tests (see Methods). Decentralization significantly changed φ values from the intact state. In all three neuropeptides, φ values were different from the decentralized state, but not different from each other. Also, none of the neuropeptide states differed from the intact state, meaning that all of them essentially restored the intact values of φ.

The lack of differences in the pyloric phase relationships among different peptide bath applications goes contrary to the idea that neuropeptides with convergent cellular actions that target different subsets of circuit neurons give rise to different phase relationships (Marder and Weimann, 1992; Swensen and Marder, 2001). We addressed two concerns about this finding. First, we wanted to ensure that the lack of statistical difference did not arise from insufficient

statistical power. We therefore included a larger data set from only extracellular recordings. Such recordings allow unambiguous determination of F_{cycle} and φ, but it is more difficult to obtain accurate spike counts (see Methods). Second, we wanted to ensure that consistent phase is not the automatic outcome of any neuromodulation that targets the pyloric circuit, independent of modulator identity and specific cellular and subcellular targets. We therefore included recordings obtained during bath application of DA (Fig. 5A). DA is not an unambiguously excitatory modulator, but rather has cell type-specific divergent actions on a range of ion channels and synapses (Harris-Warrick and Johnson, 2010).

In the larger data set, F_{cycle} increased from the decentralized state in all modulators, including DA (Fig. 5B). However, mean values were not substantially different from the smaller data set, and none of the modulators restored F_{cycle} to the level of the intact state. Three-dimensional plots of phases for individual data points (Fig. 5Ci, Di) and centroids (Fig. 5Cii, Dii) showed that intact and neuropeptide states cluster, while the DA state was more separated. DA responses also showed more substantial interindividual variability. Five-dimensional Euclidean distances (Δφ) between all pairs of modulatory states were statistically evaluated (Fig. 5E). As expected, decentralization significantly changed φ values from the intact state, and φ values were different from the decentralized state in all modulators, including DA. Notably, consistent with the intracellular data shown in Figure 4, the neuropeptide states were not statistically distinguishable. However, DA was significantly different from CCAP and RPCH. While PROC and RPCH were not distinguishable from the intact state, the small difference between CCAP and intact was significant. Finally, the difference between DA and intact was highly significant. Therefore, we confirmed that phase relationships were not distinguishable between different neuropeptide states and that neuropeptides returned φ to values close to, or indistinguishable from, those in the intact state. These values were not the automatic outcome of modulated states, as DA increased F_{cycle} from the decentralized state but elicited distinct phase relationships.

Multidimensional comparison shows differences in spiking attributes between neuropeptides.

Next, we analyzed the spiking behavior within bursts for the three neurons across all modulatory states, both for *#spks* (Fig. 6A) and F_{spk} (Fig. 6B). For visualization, we again plotted individual data points (Fig. 6Ai, Bi) and centroids (Fig. 6Aii, Bii). Compared to our findings for φ, in both sets of spiking attributes, modulated states appeared to cluster less, and the decentralized state was less separated from modulated states.

Figure 6Aiii shows the one-dimensional projections of Euclidean distances in the three-dimensional attribute space for *#spks* (Δ*#spks*), along with the results of statistical evaluation. Decentralization significantly altered values of *#spks*, and application of all three peptides resulted in values different from the decentralized state. Across neuropeptides, PROC differed from CCAP, but RPCH was not statistically distinguishable from either PROC or CCAP. Both CCAP and RPCH were significantly different from the intact state, while PROC was not.

Figure 6Biii shows the one-dimensional projections of Euclidean distances in the three-dimensional attribute space for F_{spk} (Δ F_{spk}), along with the results of statistical evaluation. As for *#spks,* decentralization significantly altered values of F_{spk}, and application of all three peptides resulted in values different from the decentralized state. Across neuropeptides, no significant differences were found in the direct one-to-one comparisons. However, as for *#spks*, both CCAP and RPCH were significantly different from the intact state, while PROC was not. Therefore, overall, CCAP and RPCH elicited similar spiking behavior across the three different neuron types that was different from the intact state, while PROC essentially restored the spiking behavior of the intact state.

Across all attributes, the output pattern in PROC can be distinguished from those in CCAP and RPCH.

To include all attributes into a single analysis of differences across modulatory states, we rendered them unitless by *z*-scoring (Fig. 7A, see Methods). We then calculated the Euclidean distances in 12 dimensions (F_{cycle}, 5 dimensions of φ, 3 dimensions of *#spks*, 3 dimensions of F_{spk}). Figure 7B shows the one-dimensional projections of Euclidean distances in the 12-dimensional attribute space for *z*-scored values (Δ*z*-scores), along with the results of statistical evaluation. The decentralized state was significantly different from the intact state, and all neuropeptide states were significantly different from the decentralized state. Across neuropeptides, PROC was significantly different from CCAP and RPCH, but the difference between CCAP and RPCH was not significant. None of the neuropeptides fully recovered the output

pattern, as all were significantly different from the intact state. This included PROC, which was indistinguishable from the intact state in the separate analyses of φ (Fig. 4C), *#spks* (Fig. 6Aiv), and F_{spk} (Fig. 6Biv). However, this is likely explained by the fact that the difference between PROC and the intact state was highly significant in the separate analysis of F_{cycle} (Fig. 2B).

As an alternative way to visualize the differences between modulatory states, we performed PCA on the *z*-scored 12-dimensional data. In the dimensions of the first three principal components (Fig. 7C), which accounted for 73.4% of the variance, decentralization moved the output pattern to substantially different coordinates. Upon application of a modulator, PROC moved the pattern relatively close to the original intact state, while CCAP and RPCH were more distant from the intact state. Figure 7D depicts how the output pattern changes along those different principal components. Along PC1, the largest contribution to pattern changes was F_{cycle}, followed by F_{spk} in all neurons and a subset of phases (φLP_{off}, φPY_{on}, φPD_{off}). Along PC2 and PC3, the largest contributions were from LP *#spks* and φLP_{on}, respectively.

From all separate and joint analyses of output pattern attributes, we conclude that CCAP and RPCH elicit similar output patterns in the pyloric circuit, while PROC elicits a distinct pattern that is closer to the intact state than the ones elicited by CCAP or RPCH.

Machine learning confirms the differences between neuropeptide-elicited output patterns.

All analyses shown so far were based on attributes that are well-established for the quantification of rhythmic circuit output but are ultimately an arbitrary subset of measures that can be taken from the recording traces. We therefore asked the question how well patterns could be distinguished with a less biased approach. To this end, we employed machine learning algorithms that were trained on a subset of data from each modulatory state and then used to blindly classify output patterns by modulatory state. The general idea was to ask how successful the algorithm is in correctly identifying a modulatory state across a selection of given individual output patterns.

For a direct initial comparison with our attribute-based approach, we first used a pattern recognition network (Fig. 8A) that solely relied on the same selected attributes we extracted from the recordings, namely the 12-dimensional *z*-score values used in Figure 7. Figure 8B shows the classification matrix from this approach. A high percentage of data from the intact and decentralized states were correctly classified, with error rates of <10%. The algorithm also classified most neuropeptide states correctly but had a much higher error rate for each. Misclassifications corresponded reasonably well with our results from determining Euclidean distances in some cases, but less so in others. CCAP and RPCH (which were statistically indistinguishable) had the largest percentages of misclassifications as each other, meaning these two states were easily confused. PROC was often misclassified as the intact state (which it was statistically indistinguishable from), but also as RPCH.

To rely less on predetermined attributes, we performed a more minimal analysis by extracting spike times of each neuron and sorting them into a fixed number of bins per cycle. Figure 8C shows an example of a spike phase histogram constructed with this approach. Because solely relying on *#spks*/bin does not account for differences in F_{cycle} between modulatory states, we subsequently added the *z*-scored F_{cycle} values to the bin counts. We used these data to train a time series classification network (Fig. 8D). Overall, classifications were less successful than with the pattern recognition network. Furthermore, error rates were larger when we used only the *#spks*/bin values (Fig. 8E) than when we added *z*-scored F_{cycle} values (Fig. 8F). With F_{cycle} included, classifications were highly successful for the intact state, and still had a relatively low error rate for the decentralized state. PROC had the highest error rate and curiously was more often confused with the decentralized state than the intact state. Again, the largest percentage of misclassifications for CCAP and RPCH was as each other, meaning these two states were still easily confused. Except for PROC, the algorithm recognized the correct modulatory state in the majority of cases, but also had relatively high error rates for the other two neuropeptides. Overall, the findings of the two ML analyses are consistent with our Euclidean distance analysis.

Discussion

Neuromodulators that are convergent in some of their downstream intracellular targets could have distinct actions at the level of neural circuits due to the fact that different circuit neuron types express different modulatory receptors.

Swensen and Marder (2001) showed this circuit-level divergence schematically by highlighting how different peptides elicit the modulatory current I_{MI} in different pyloric neurons (simplified in the top row of our Fig. 2A). Interestingly, the findings that output patterns in PROC are most similar to the state with intact descending inputs, and that output patterns in CCAP and RPCH are statistically indistinguishable match well with these schematics. Although all three peptides we examined target AB and LP, both CCAP and RPCH only target these two neurons but not the PD and PY neurons that are targeted by PROC. Thus, the distinctions between these peptides at the level of the single-neuron output attributes was clearly reflected in the PY and PD bursting activity: CCAP differed from PROC in PY spike numbers per burst, whereas RPCH differed with PROC in PY intraburst spike frequency. All three peptides also differed in their effect on the PD spike numbers. These findings are consistent with the results of the Swensen and Marder (2001) study, which elegantly demonstrated that the dynamic clamp addition of I_{MI} to PD and PY, the neurons that PROC targets and CCAP does not, removes the distinction between the PY and PD intraburst spiking between these two neurons.

All our statistical comparisons were done with unpaired experimental paradigms. It is possible that output patterns across different neuropeptides are better distinguishable in individual preparations and that interindividual variability masked differences in our analysis. In fact, in the Swensen and Marder (2001) mentioned above, a paired comparison (sequential applications in each experiment) of output patterns in PROC and CCAP and found significant differences in φPD_{off} and φPY_{off} that we did not detect here (Fig. 2C). This is an important distinction highlighting the goal of our study to understand the unbiased distribution of pyloric activity patterns elicited by each neuropeptide compared to exploring actions of each peptide on specific output attributes within the same preparation.

The core pyloric circuit consists of the AB/PD, LP and PY neurons on which we focused in this study. However, the STG also includes the gastric mill CPG which involves multiple neuron types and controls the movement of the teeth, as well as the inferior cardiac (IC) and ventral dilator (VD) neurons that participate in both pyloric and gastric mill activity patterns. The three peptides that we examined here also influence some of these other neurons with a distinct pattern. For example, PROC activates I_{MI} in both the VD and the IC neuron, CCAP activates I_{MI} in the IC neuron, while RPCH does not target either of these two neurons (Swensen and Marder, 2001). Although, due to the limitations of our experimental protocols, we did not include all STG gastro-pyloric neurons in our analysis, a complete map of the actions of the three peptides should also include their effects on other STG neurons.

It is noteworthy that intact modulatory inputs are under control of multiple modulators (including monoamines and other non-peptides), and effects of different modulators can differ quantitatively and are not necessarily simply additive (Li et al., 2018). The presence of additional modulators partly explains why none of the three peptides we examined produce a pattern identical to that of the intact circuit, as is quite clear from the differences in the cycle frequency and the PD neuron spike frequency.

Many excitatory neuropeptides as well as muscarinic agonists are known to converge to activate IMI (Swensen and Marder, 2000, 2001) in pyloric neurons, although I_{MI} is now known to consist of at least two components (Rodriguez et al., 2013; Schneider et al., 2021). However, many of these peptides also influence synaptic efficacy in the STG, mainly by enhancing synaptic strength (Thirumalai et al., 2006; Atamturktur and Nadim, 2011; Garcia et al., 2015; Li et al., 2018), but also synaptic dynamics (Zhao et al., 2011). Compared to the actions of peptides on voltage-gated ionic currents, the effects on pyloric synapses are only partially studied, but it is possible that some of the synaptic effects may also be due to the permeability of I_{MI} channels to calcium (Zhao et al., 2011; Oh et al., 2012; Schneider et al., 2021).

In a recurrent circuit, all output pattern attributes are potentially interdependent. However, some commonly quantified attributes that we measured in this study are unambiguously redundant. These include the burst phases since, for instance, the burst end obviously follows the burst onset and the sequence of firing of neurons is mainly determined by their synaptic interactions. In fact, a main reason for not using burst latency instead of burst phase (latency x cycle period) is that latency is primarily determined by cycle period whereas burst phase is independent of period (Fig. 3A). Additionally, some interdependence is between attributes that have different units, such as phase and frequency. By using *z*-score values, we do not ignore the interdependence of attributes nor the fact that these attributes may have different units. The redundancy of the attributes is also reflected in the principal component analysis of the *z*-score

vectors, since the first three principal components account for > 73% of the variability (Fig. 7C). The multivariate permutation test provides a reliable statistical comparison between the *z*-scored vectors (Anderson, 2001; Nichols and Holmes, 2002) without bias for specific attributes. We argue that this is an unbiased way of comparing the circuit outputs because there is no *a priori* way of knowing which attributes may be the most salient features of the motor output pattern. This is well justified by the muscle readout of patterned pyloric activity. Daur et al (2021) show that of the two muscle types that are targets of the PD neuron, one is moderately sensitive to changes in either F_{cycle} or PD F_{spk}, whereas the other is insensitive to F_{cycle} but is acutely sensitive to PD F_{spk}. The multivariate permutation test, as many statistical hypothesis tests, indicates the probability of distributions having equal population means, but does not inform how different the two population means may be. To provide a measure of this distance we used a simple Euclidean distance of the population centroids which provides a useful geometric description. For instance, the PROC motor output is much closer to the intact rhythm than the RPCH or CCAP outputs, which are both as far from the intact rhythm as the decentralized unmodulated rhythm.

As mentioned, the burst latency of different pyloric neurons is strongly correlated with the cycle period or, equivalently, phase remains relatively independent of F_{cycle} across animals (Fig. 3A) (Bucher et al., 2005; Goaillard et al., 2009; Anwar et al., 2022). A previous study showed that, with decentralization, this phase constancy falls apart and phases vary substantially with F_{cycle}, but relatively normal and stable phase relationships recover over the course of many hours (Luther et al., 2003). Therefore, as we also find (Fig. 3A), decentralized circuits did not just differ in absolute values of phases but lost their ability to maintain phases across different values of F_{cycle}. Luther et al (2003) predicted that inter-animal phase constancy in the intact pyloric circuit requires the presence of neuromodulation. Our data directly support this hypothesis, but we additionally find that all three peptides recover the same phase relationships as those seen in the intact circuit (Fig. 3A).

Why do the peptide patterns not differ in phase? One possibility is that pyloric phases are mainly determined by the activity of the pacemaker neurons. All three peptides act on the pacemaker AB neuron and produce similar F_{cycle} and φPDoff (pacemaker end phase) values. For the LP and PY neurons to have different phases with different peptides, their latencies would have to be different. Both neuron types, however, burst on rebound from pacemaker inhibition. It has been suggested that the voltage-dependence of I_{MI} results in rebound timing that changes proportionally to the duration of inhibition (i.e. the AB/PD burst duration) and therefore the rebound phase is relatively unaffected (Schneider et al., 2021). This does not mean that the activity phases of follower neurons are altogether unaffected by neuromodulation, as bath application of monoamines has a strong effect on these phases (Harris-Warrick and Johnson, 2010).

References

Anderson MJ (2001) Permutation tests for univariate or multivariate analysis of variance and regression. Canadian Journal of Fisheries and Aquatic Sciences 58:626-639.

Anwar H, Martinez D, Bucher D, Nadim F (2022) Inter-Animal Variability in Activity Phase Is Constrained by Synaptic Dynamics in an Oscillatory Network. eNeuro 9.

Atamturktur S, Nadim F (2011) Effects of neuromodulator RPCH on short-term dynamics of a key synapse in an oscillatory network of crab Cancer borealis. J Appl Biol Sci 5:59-72.

Bucher D, Marder E (2013) SnapShot: Neuromodulation. Cell 155:482-482 e481.

Bucher D, Prinz AA, Marder E (2005) Animal-to-animal variability in motor pattern production in adults and during growth. J Neurosci 25:1611-1619.

Calabrese RL, Norris BJ, Wenning A, Wright TM (2011) Coping with variability in small neuronal networks. Integr Comp Biol 51:845-855.

Daur N, Nadim F, Bucher D (2016) The complexity of small circuits: the stomatogastric nervous system. Curr Opin Neurobiol 41:1-7.

Daur N, Nadim F, Bucher D (2021) Synaptic dynamics convey differential sensitivity to input pattern changes in two muscles innervated by the same motor neurons. eNeuro 8.

Diaz-Rios M, Guertin PA, Rivera-Oliver M (2017) Neuromodulation of Spinal Locomotor Networks in Rodents. Current pharmaceutical design 23:1741-1752.

Doi A, Ramirez JM (2008) Neuromodulation and the orchestration of the respiratory rhythm. Respir Physiol Neurobiol 164:96-104.
Due MR, Wang Y, Barry MA, Jing J, Reaver CN, Weiss KR, Cropper EC (2022) Convergent effects of neuropeptides on the feeding central pattern generator of Aplysia californica. J Neurophysiol 127:1445-1459.
Garcia VJ, Daur N, Temporal S, Schulz DJ, Bucher D (2015) Neuropeptide receptor transcript expression levels and magnitude of ionic current responses show cell type-specific differences in a small motor circuit. J Neurosci 35:6786-6800.
Goaillard JM, Marder E (2021) Ion Channel Degeneracy, Variability, and Covariation in Neuron and Circuit Resilience. Annu Rev Neurosci 44:335-357.
Goaillard JM, Taylor AL, Schulz DJ, Marder E (2009) Functional consequences of animal-to-animal variation in circuit parameters. Nat Neurosci 12:1424-1430.
Golowasch J (2014) Ionic Current Variability and Functional Stability in the Nervous System. Bioscience 64:570-580.
Golowasch J, Marder E (1992) Proctolin activates an inward current whose voltage dependence is modified by extracellular Ca2+. J Neurosci 12:810-817.
Goodfellow I, Bengio Y, Courville A (2016) Deep learning. Cambridge, Massachusetts: The MIT Press.
Gray M, Golowasch J (2016) Voltage Dependence of a Neuromodulator-Activated Ionic Current. eNeuro 3.
Gray M, Daudelin DH, Golowasch J (2017) Activation mechanism of a neuromodulator-gated pacemaker ionic current. J Neurophysiol 118:595-609.
Grillner S (2006) Biological pattern generation: the cellular and computational logic of networks in motion. Neuron 52:751-766.
Hamood AW, Marder E (2014) Animal-to-Animal Variability in Neuromodulation and Circuit Function. Cold Spring Harb Symp Quant Biol 79:21-28.
Harris-Warrick RM (2011) Neuromodulation and flexibility in Central Pattern Generator networks. Curr Opin Neurobiol 21:685-692.
Harris-Warrick RM, Johnson BR (2010) Checks and balances in neuromodulation. Front Behav Neurosci 4.
Hooper SL (1997) Phase maintenance in the pyloric pattern of the lobster (*Panulirus interruptus*) stomatogastric ganglion. J Comput Neurosci 4:191-205.
Janiesch C, Zschech P, Heinrich K (2021) Machine learning and deep learning. Electronic Markets 31:685-695.
Jones BE (2020) Arousal and sleep circuits. Neuropsychopharmacology 45:6-20.
Le Gal JP, Dubuc R, Smarandache-Wellmann C (2017) Coordination of Rhythmic Movements. In: Neurobiology of Motor Control: Fundamental Concepts and New Directions (Hooper SL, Buschges A, eds). Hoboken, New Jersey: Wiley-Blackwell.
Li X, Bucher D, Nadim F (2018) Distinct Co-Modulation Rules of Synapses and Voltage-Gated Currents Coordinate Interactions of Multiple Neuromodulators. J Neurosci 38:8549-8562.
Luther JA, Robie AA, Yarotsky J, Reina C, Marder E, Golowasch J (2003) Episodic bouts of activity accompany recovery of rhythmic output by a neuromodulator- and activity-deprived adult neural network. J Neurophysiol 90:2720-2730.
Maloney RT (2021) Neuromodulation and Individuality. Front Behav Neurosci 15:777873.
Marder E (2012) Neuromodulation of neuronal circuits: back to the future. Neuron 76:1-11.
Marder E, Weimann JM (1992) Modulatory control of multiple task processing in the stomatogastric nervous system. In: Neurobiology of Motor Progamme Selection (Kien J, McCrohan C, Winlow B, eds), pp 3-19. New York: Pergamon Press.
Marder E, Goaillard JM (2006) Variability, compensation and homeostasis in neuron and network function. Nat Rev Neurosci 7:563-574.
Marder E, Bucher D (2007) Understanding circuit dynamics using the stomatogastric nervous system of lobsters and crabs. Annu Rev Physiol 69:291-316.
Marder E, Tobin AE, Grashow R (2007) How tightly tuned are network parameters? Insight from computational and experimental studies in small rhythmic motor networks. Prog Brain Res 165:193-200.
Marder E, O'Leary T, Shruti S (2014a) Neuromodulation of circuits with variable parameters: single neurons and small circuits reveal principles of state-dependent and robust neuromodulation. Annu Rev Neurosci 37:329-346.
Marder E, Goeritz ML, Otopalik AG (2014b) Robust circuit rhythms in small circuits arise from variable circuit components and mechanisms. Curr Opin Neurobiol 31C:156-163.

Maynard DM, Dando MR (1974) The structure of the stomatogastric neuromuscular system in *Callinectes sapidus, Homarus americanus* and *Panulirus argus* (Decapoda Crustacea). Philos Trans R Soc Lond B 268:161-220.
McCormick DA, Williamson A (1989) Convergence and divergence of neurotransmitter action in human cerebral cortex. Proc Natl Acad Sci U S A 86:8098-8102.
McCormick DA, Nestvogel DB, He BJ (2020) Neuromodulation of Brain State and Behavior. Annu Rev Neurosci 43:391-415.
Mullins OJ, Hackett JT, Buchanan JT, Friesen WO (2011) Neuronal control of swimming behavior: comparison of vertebrate and invertebrate model systems. Prog Neurobiol 93:244-269.
Nadim F, Bucher D (2014) Neuromodulation of neurons and synapses. Curr Opin Neurobiol 29C:48-56.
Nichols TE, Holmes AP (2002) Nonparametric permutation tests for functional neuroimaging: a primer with examples. Hum Brain Mapp 15:1-25.
Oh M, Zhao S, Matveev V, Nadim F (2012) Neuromodulatory changes in short-term synaptic dynamics may be mediated by two distinct mechanisms of presynaptic calcium entry. J Comput Neurosci 33:573-585.
Rodriguez JC, Blitz DM, Nusbaum MP (2013) Convergent rhythm generation from divergent cellular mechanisms. J Neurosci 33:18047-18064.
Schneider AC, Itani O, Bucher D, Nadim F (2022) Neuromodulation reduces interindividual variability of neuronal output. eNeuro 9.
Schneider AC, Fox D, Itani O, Golowasch J, Bucher D, Nadim F (2021) Frequency-Dependent Action of Neuromodulation. eNeuro 8.
Schuster M, Paliwal KK (1997) Bidirectional recurrent neural networks. IEEE Trans Signal Process 45:2673-2681.
Soofi W, Goeritz ML, Kispersky TJ, Prinz AA, Marder E, Stein W (2014) Phase maintenance in a rhythmic motor pattern during temperature changes in vivo. J Neurophysiol 111:2603-2613.
Stein W (2009) Modulation of stomatogastric rhythms. J Comp Physiol A Neuroethol Sens Neural Behav Physiol 195:989-1009.
Swensen AM, Marder E (2000) Multiple peptides converge to activate the same voltage-dependent current in a central pattern-generating circuit. J Neurosci 20:6752-6759.
Swensen AM, Marder E (2001) Modulators with convergent cellular actions elicit distinct circuit outputs. J Neurosci 21:4050-4058.
Tamvacakis AN, Lillvis JL, Sakurai A, Katz PS (2022) The Consistency of Gastropod Identified Neurons Distinguishes Intra-Individual Plasticity From Inter-Individual Variability in Neural Circuits. Front Behav Neurosci 16:855235.
Tang LS, Taylor AL, Rinberg A, Marder E (2012) Robustness of a rhythmic circuit to short- and long-term temperature changes. J Neurosci 32:10075-10085.
Thirumalai V, Prinz AA, Johnson CD, Marder E (2006) Red pigment concentrating hormone strongly enhances the strength of the feedback to the pyloric rhythm oscillator but has little effect on pyloric rhythm period. J Neurophysiol 95:1762-1770.
Vidal-Gadea A, Topper S, Young L, Crisp A, Kressin L, Elbel E, Maples T, Brauner M, Erbguth K, Axelrod A, Gottschalk A, Siegel D, Pierce-Shimomura JT (2011) Caenorhabditis elegans selects distinct crawling and swimming gaits via dopamine and serotonin. Proc Natl Acad Sci U S A 108:17504-17509.
Xu J, Lopez AJ, Hoque MM, Borich MR, Kesar TM (2021) Temporal Profile of Descending Cortical Modulation of Spinal Excitability: Group and Individual-Specific Effects. Front Integr Neurosci 15:777741.
Zhang C, Guy RD, Mulloney B, Zhang Q, Lewis TJ (2014) Neural mechanism of optimal limb coordination in crustacean swimming. Proc Natl Acad Sci U S A 111:13840-13845.
Zhao S, Sheibanie AF, Oh M, Rabbah P, Nadim F (2011) Peptide neuromodulation of synaptic dynamics in an oscillatory network. J Neurosci 31:13991-14004.

Figure Legends

Figure 1: Experimental preparation and example recording traces. **A:** Schematic of the isolated STNS with three intracellular recording electrodes in the STG. CoG: commissural ganglion; OG: esophageal ganglion; stn: stomatogastric nerve; STG: stomatogastric ganglion; lvn: lateral ventricular nerve; pdn: pyloric dilator nerve; pyn: pyloric nerve. Nomenclature after Maynard and Dando (1974). **B:** Simplified pyloric circuit diagram (inset) and example traces from simultaneous intracellular soma recordings and extracellular nerve recordings, indicating the output pattern attributes used for analyses. Ball-and-stick connections in the inset indicate synaptic inhibition, whereas resistor symbols indicate electrical coupling. Multiple circles indicate multiple copies of that neuron type.

Figure 2: Comparison of circuit output patterns under different neuromodulatory conditions. **A:** Example traces from a single preparation under different modulatory conditions. In the circuit diagrams, neurons and synapses are shown in color if they are modulated in a given condition, and in white if they are not modulated (see main text for references). Synaptic connections for which there is no available information about modulation are gray and marked with question marks. **B:** Means (bars) and individual data points (circles) for F_{cycle} (intact: n = 43; decentralized: n = 46; PROC: n = 15; CCAP: n = 18; RPCH: n = 19). One-way ANOVA showed significant difference between treatments ($F_{(4,140)} = 101.3$, $p < 0.001$, power = 1, normality and equal variance tests passed). Asterisks indicate significant differences determined by subsequent Holm-Sidak post-hoc tests. **C:** Mean values of φ (bars) and individual data points (filled circles: φ_{on}, open circles: φ_{off}). Two-way ANOVA showed significant interactions ($F_{(16,704)} = 15.7$, $p < 0.001$, power = 1, normality and equal variance tests failed). Asterisks indicate significant difference determined by subsequent Holm-Sidak post-hoc tests. **D:** Means (bars) and individual data points (circles) for *#spks*. Two-way ANOVA showed significant interactions ($F_{(8,422)} = 26.1$, $p < 0.001$, power = 1, normality and equal variance tests failed). Asterisks indicate significant differences determined by subsequent Holm-Sidak post-hoc tests. **E:** Means (bars) and individual data points (circles) for F_{spk}. Two-way ANOVA showed significant interactions ($F_{(8,422)} = 6.4$, $p < 0.001$, power = 1, normality and equal variance tests passed). Asterisks indicate significant differences determined by subsequent Holm-Sidak post-hoc tests.

Figure 3: Dependence of burst and spike attributes on P or F_{cycle}. **A:** Plot and regression of latencies vs. P, and φ vs. F_{cycle}, for all the combined modulated states (intact, PROC, CCAP, RPCH; upper panels) and the decentralized state (lower panels). Points with black edges indicate mean values. **B:** Regression of *#spks* vs. P for all combined states in the three neuron types. **C:** Regression of F_{spk} vs. F_{cycle} for all combined states in the three neuron types.

Figure 4: Euclidean distance analysis of phase relationships. Data set is the same as shown in Figure 2. **A:** Three-dimensional plots (spheres) and corresponding two-dimensional projections (grids) of three of the five phases (φLP_{on}, φLP_{off}, and φPY_{on}), for individual experiments (i) and centroids (ii). Lines connecting the centroids represent the Euclidean distances in three dimensions. **B:** Plots of different combinations of three of the five phases (φPD_{off}, φLP_{off}, φPY_{off}). **C:** One-dimensional projections of the five-dimensional Euclidean distances (Δφ) between all modulatory states. Significance of differences between different modulatory states was determined with multivariate permutation tests.

Figure 5: Analysis of F_{cycle} and φ in a large data set from extracellular recordings, including DA (intact: n = 105; decentralized: n = 100; PROC: n = 28; CCAP: n = 34; RPCH: n = 36; DA: n = 15). **A:** Example extracellular recording traces from a single preparation after decentralization and after application of DA. **B:** Means and individual data points for F_{cycle}. One-way ANOVA showed significant difference between treatments ($F_{(5,317)} = 150.7$, $p < 0.001$, power = 1, normality and equal variance tests passed). Asterisks indicate significant differences determined by subsequent Holm-Sidak post-hoc tests. **C:** Three-dimensional plots (spheres) and corresponding two-dimensional projections (grids) of three of the five phases (φLP_{on}, φLP_{off}, and φPY_{on}), for individual experiments (i) and centroids (ii). Lines connecting the centroids represent the Euclidean distances in three dimensions. **D:** Plots of different combinations of three of the five phases (φPD_{off}, φLP_{off}, φPY_{off}). **E:** One-dimensional projections of the five-dimensional Euclidean distances (Δφ) between all modulatory states. Significance of differences between different modulatory states was determined with multivariate permutation tests.

Figure 6: Euclidean distance analysis of spiking behavior. Data set is the same as shown in Figure 2. **A:** Analysis of number of spikes per burst in all three neurons.Three-dimensional plots (spheres) and corresponding two-dimensional

projections (grids) for individual experiments (i) and centroids (ii). Lines connecting the centroids represent the Euclidean distances in three dimensions. One-dimensional projections of the Euclidean distances (Δ*#spks*) between all modulatory states (iii) are shown with the results of multivariate permutation tests. **B:** Same analysis as in **A**, but for spike frequencies within bursts in all three neurons.

Figure 7: Euclidean distance analysis including all 12 output pattern attributes. **A:** Individual data points for all attributes, *z*-scored across all modulatory states. Means are shown as thick lines. **B:** One-dimensional projections of the 12-dimensional Euclidean distances (Δ*z*-scores) between all modulatory states. Significance was determined with multivariate permutation tests. **C:** Different modulatory states as centroids (spheres) and distances (dashed lines) in the dimensions of the first three principal components obtained by PCA. **D:** Theoretical change of output patterns along the first three principal components, in the range of ±2 standard deviations.

Figure 8: Classification of modulatory states with machine learning algorithms. **A:** Schematic of the pattern recognition network architecture (see Methods) trained to classify modulatory states from the same circuit output pattern attributes used for the 12-dimensional Euclidean distance analysis shown in Figure 7. **B:** Classification matrix of the results from the pattern recognition network. The true class is the actual modulatory state and the predicted class the identification result. Percentages of predicted classes for each true class are represented by the areas within circles. The number values of correct classifications represent the percentages along each true class row. Areas inside the dashed circles represent 100%, the size of the circle if all experiments were classified correctly. Because of the unequal numbers of experiments in each true class, the sum of circle areas add up to 100% only within each row. **C:** Example of spike timing of PD, LP, and PY in two consecutive normalized cycles, and example spike phase histogram from mean spike counts across all cycles in a 30s recording. Mean *#spks*/bin were both used as they were (left scale) and after adding the F_{cycle} *z*-score value (right scale). **D:** Simplified schematic of the time series classification network architecture (see Methods) trained to classify modulatory states from the spike phase histograms. **E:** Classification matrix from phase histograms of mean *#spks*/bin values. **F:** Classification matrix from phase histograms of mean *#spks*/bin values offset by F_{cycle} *z*-score values.

x	y	Treatment	Normality (Shapiro-Wilk)	Const. variance	Degrees of freedom (regression; total)	F	t (y_0)	p (y_0)	t (slope)	p (slope)	R	R^2
P	$\Delta t\ PD_{off}$	modulated	failed	failed	1;94	33.82	3.901	0.0002	5.816	<0.0001	0.52	0.27
P	$\Delta t\ LP_{on}$	modulated	passed	passed	1;94	226.83	2.882	0.0049	15.061	<0.0001	0.84	0.71
P	$\Delta t\ LP_{off}$	modulated	failed	failed	1;94	794.88	-0.927	0.3562	28.194	<0.0001	0.95	0.9
P	$\Delta t\ PY_{on}$	modulated	passed	failed	1;94	249.55	0.443	0.6589	15.797	<0.0001	0.85	0.73
P	$\Delta t\ PY_{off}$	modulated	passed	failed	1;94	5264.54	1.115	0.2678	72.557	<0.0001	0.99	0.98
F_{cycle}	φPD_{off}	modulated	passed	passed	1;94	17.64	5.884	<0.0001	4.2	<0.0001	0.40	0.16
F_{cycle}	φLP_{on}	modulated	passed	passed	1;94	6.25	14.289	<0.0001	2.5	0.0142	0.25	0.06
F_{cycle}	φLP_{off}	modulated	passed	passed	1;94	0.81	28.614	<0.0001	-0.898	0.3713	0.09	0.01
F_{cycle}	φPY_{on}	modulated	passed	passed	1;94	1.24	14.069	<0.0001	1.114	0.2682	0.12	0.01
F_{cycle}	φPY_{off}	modulated	passed	passed	1;94	0.54	67.441	<0.0001	0.732	0.4662	0.08	0.01
P	$\Delta t\ PD_{off}$	decentralized	passed	passed	1;45	0.5	6.779	<0.0001	0.71	0.4818	0.11	0.01
P	$\Delta t\ LP_{on}$	decentralized	passed	passed	1;45	13.7	5.324	<0.0001	3.702	0.0006	0.49	0.24
P	$\Delta t\ LP_{off}$	decentralized	passed	passed	1;45	7.56	8.357	<0.0001	2.75	0.0086	0.38	0.15
P	$\Delta t\ PY_{on}$	decentralized	passed	passed	1;45	4.97	7.245	<0.0001	2.23	0.0309	0.32	0.10
P	$\Delta t\ PY_{off}$	decentralized	failed	passed	1;45	2669.87	0.131	0.8964	51.671	<0.0001	0.99	0.98
F_{cycle}	φPD_{off}	decentralized	passed	passed	1;45	23.16	1.719	0.0926	4.813	<0.0001	0.59	0.34
F_{cycle}	φLP_{on}	decentralized	passed	passed	1;45	13.05	4.381	<0.0001	3.613	0.0008	0.48	0.23
F_{cycle}	φLP_{off}	decentralized	passed	passed	1;45	42.86	3.676	0.0006	6.547	<0.0001	0.70	0.49
F_{cycle}	φPY_{on}	decentralized	passed	passed	1;45	27.57	3.088	0.0035	5.251	<0.0001	0.62	0.39
F_{cycle}	φPY_{off}	decentralized	failed	passed	1;45	0.15	42.588	<0.0001	0.388	0.7002	0.06	0.00
P	*#spks* PD	all	passed	passed	1;140	39.25	15.889	<0.0001	-6.265	<0.0001	0.47	0.22
P	*#spks* LP	all	failed	failed	1;140	9.9	11.122	<0.0001	-3.147	0.002	0.26	0.07
P	*#spks* PY	all	failed	failed	1;140	5.27	5.684	<0.0001	2.296	0.0232	0.19	0.04
F_{cycle}	F_{spk} PD	all	passed	failed	1;140	228.6	-4.492	<0.0001	15.119	<0.0001	0.79	0.62
F_{cycle}	F_{spk} LP	all	passed	failed	1;140	141.9	0.363	0.7172	11.912	<0.0001	0.71	0.51
F_{cycle}	F_{spk} PY	all	failed	passed	1;140	192.78	0.425	0.6715	13.885	<0.0001	0.76	0.58

Table 1: Regression analysis (Fig. 3)

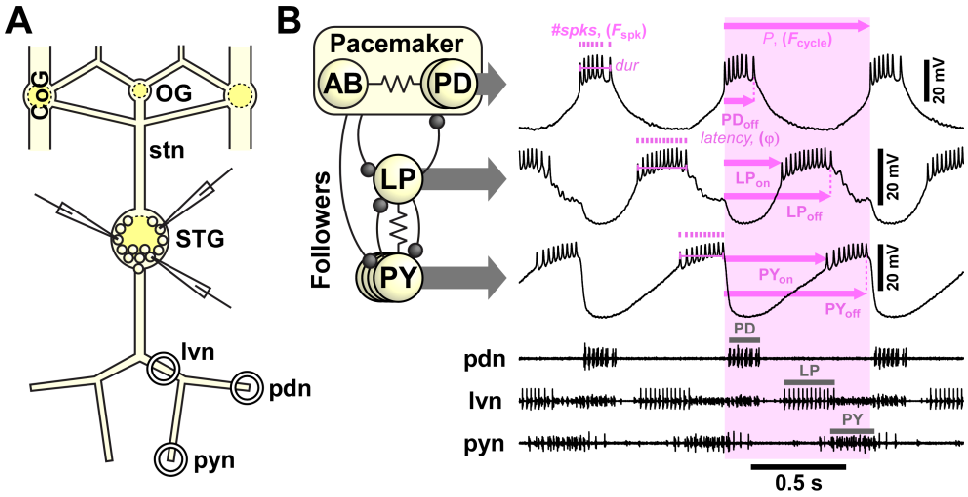
A
CoG
OG
stn
STG
lvn
pdn
pyn
B
Pacemaker
AB
PD
Followers
LP
PY
#spks, (F_{spk})
dur
P_x (F_{cycle})
PD_{off}
latency, (φ)
LP_{on}
LP_{off}
PY_{on}
PY_{off}
20 mV
20 mV
20 mV
PD
LP
PY
pdn
lvn
pyn
0.5 s

Figure 1

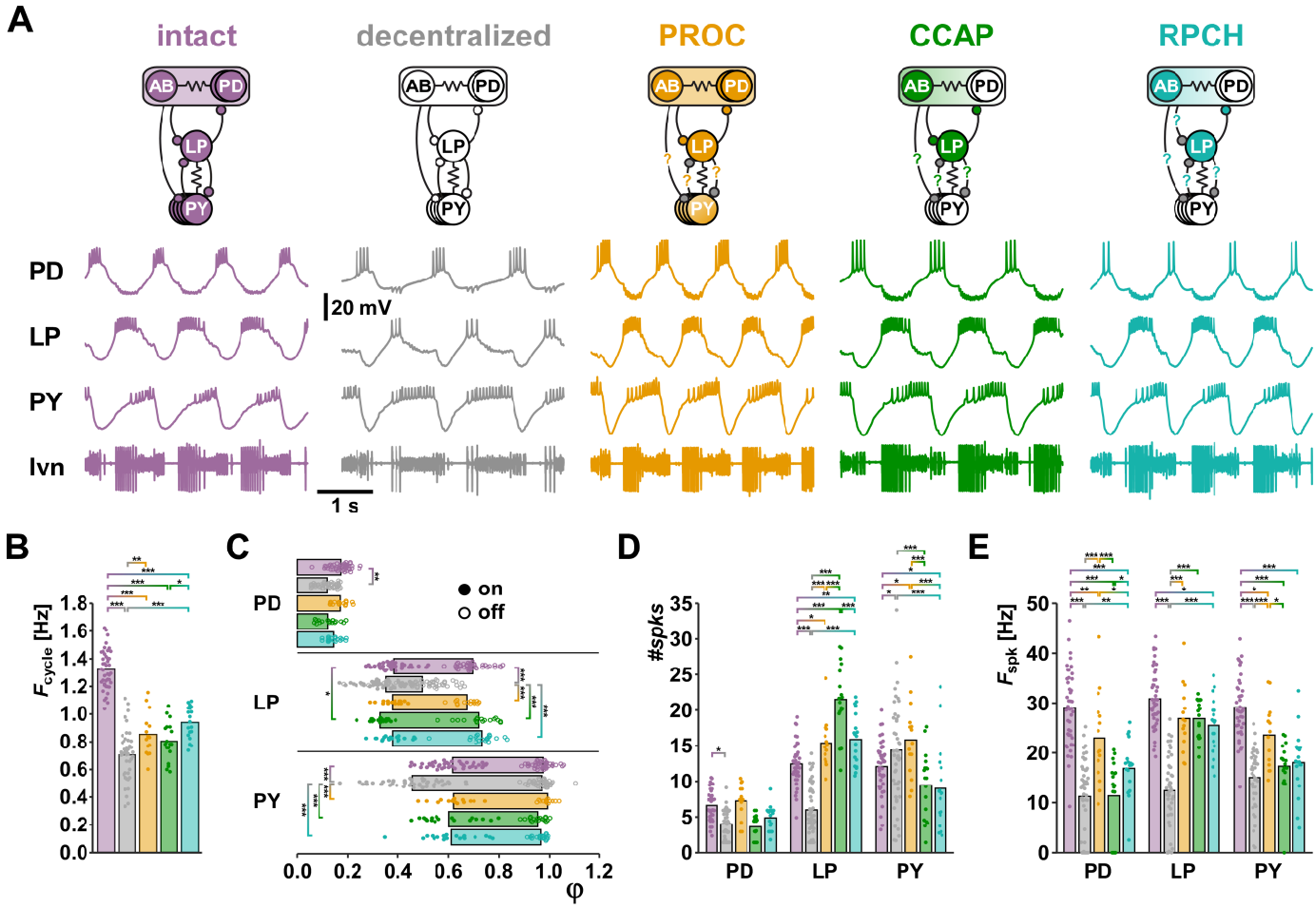
A
intact
decentralized
PROC
CCAP
RPCH
AB
PD
LP
PY
PD
LP
PY
lvn
20 mV
1 s
B
F_{cycle} [Hz]
C
PD
LP
PY
on
off
φ
D
#spks
PD
LP
PY
E
F_{spk} [Hz]
PD
LP
PY

Figure 2

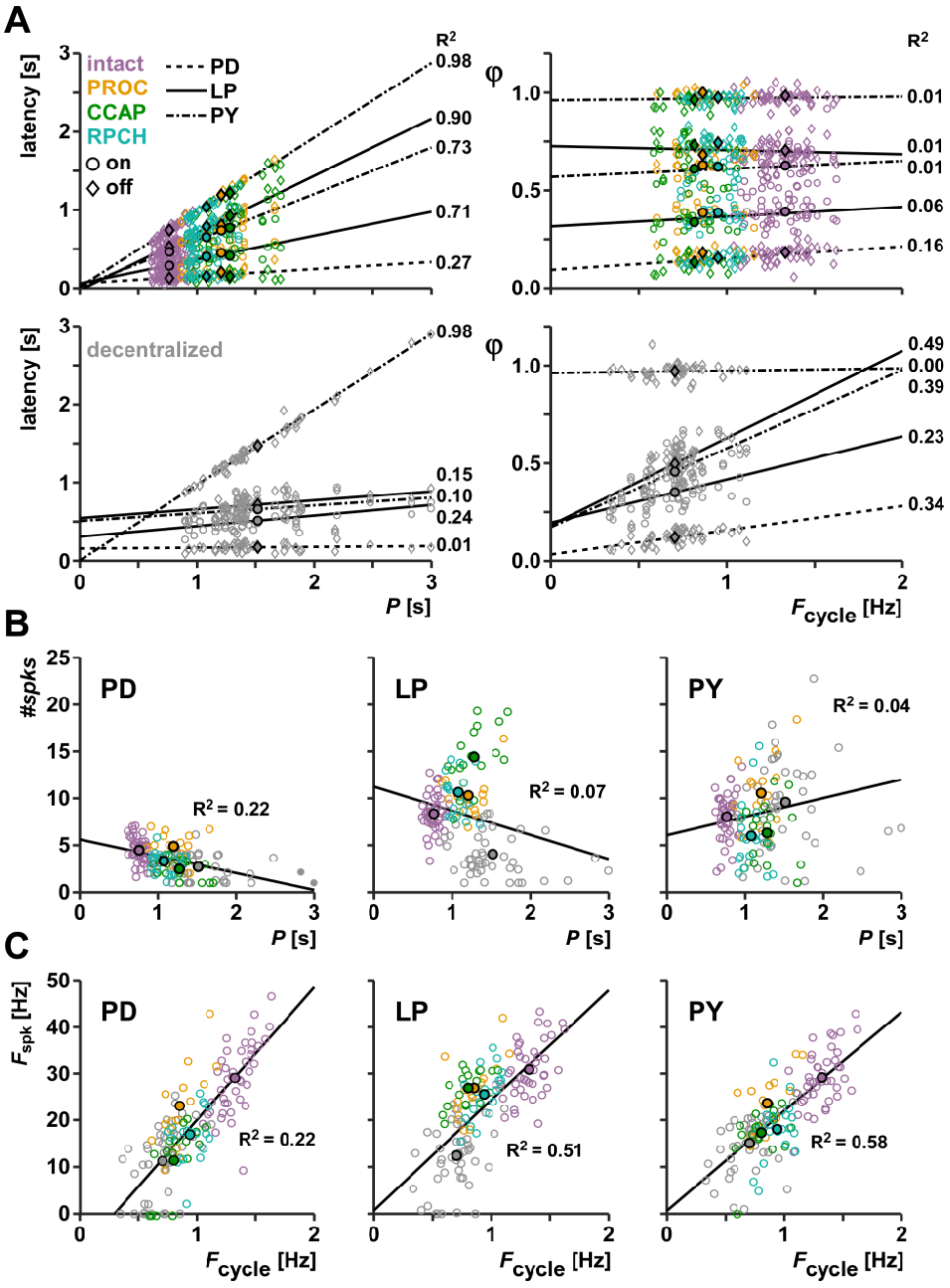
A
intact
PROC
CCAP
RPCH
on
off
PD
LP
PY
latency [s]
R²
0.98
0.90
0.73
0.71
0.27
φ
0.01
0.01
0.01
0.06
0.16
decentralized
0.15
0.10
0.24
0.01
0.49
0.00
0.39
0.23
0.34
P [s]
F_cycle [Hz]
B
#spks
PD
R² = 0.22
LP
R² = 0.07
PY
R² = 0.04
C
F_spk [Hz]
R² = 0.22
R² = 0.51
R² = 0.58

Figure 3

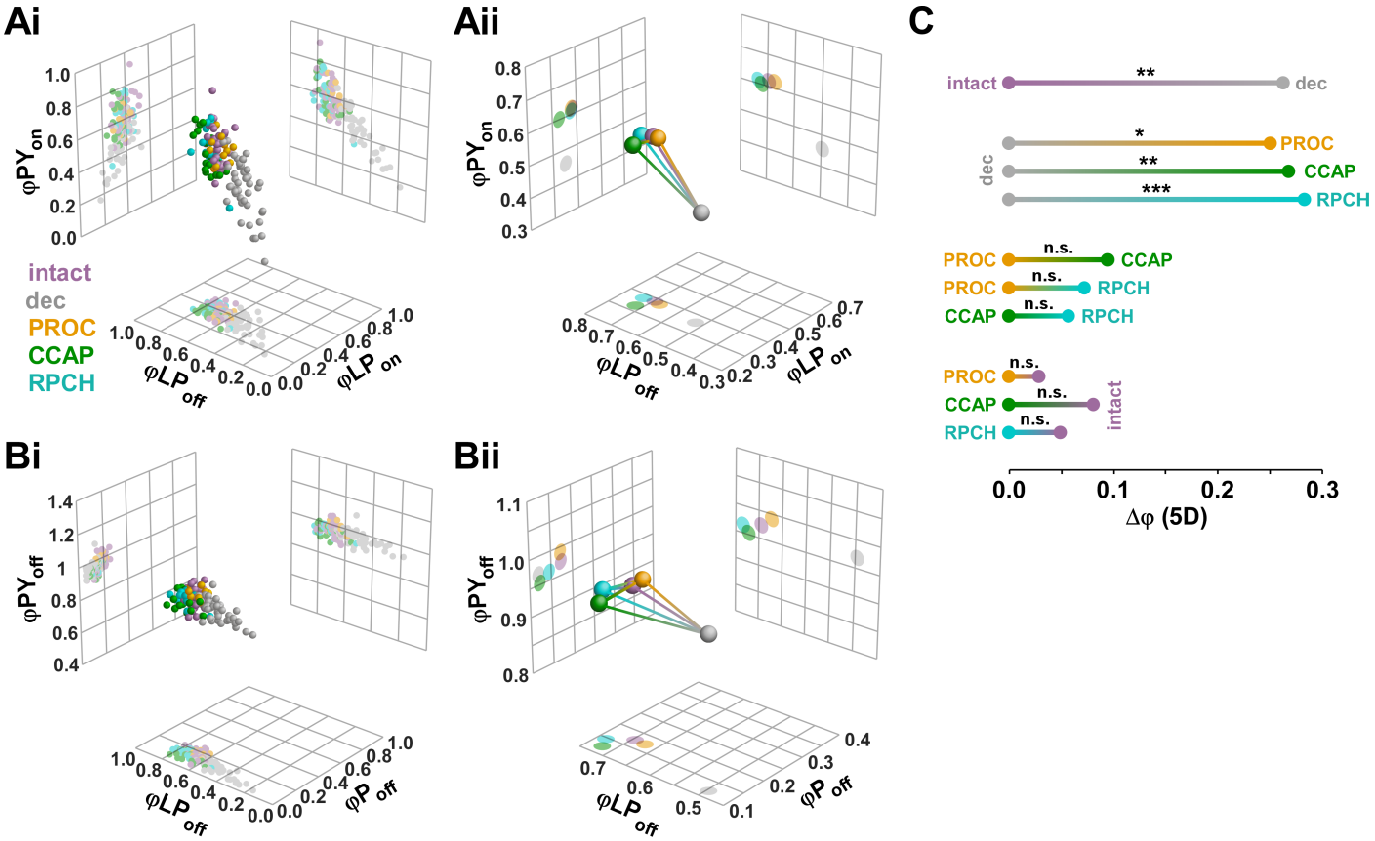
Ai
Aii
C
Bi
Bii
intact
dec
PROC
CCAP
RPCH
φPY on
φLP off
φLP on
φPY off
φP off
n.s.
*
**
***
Δφ (5D)

Figure 4

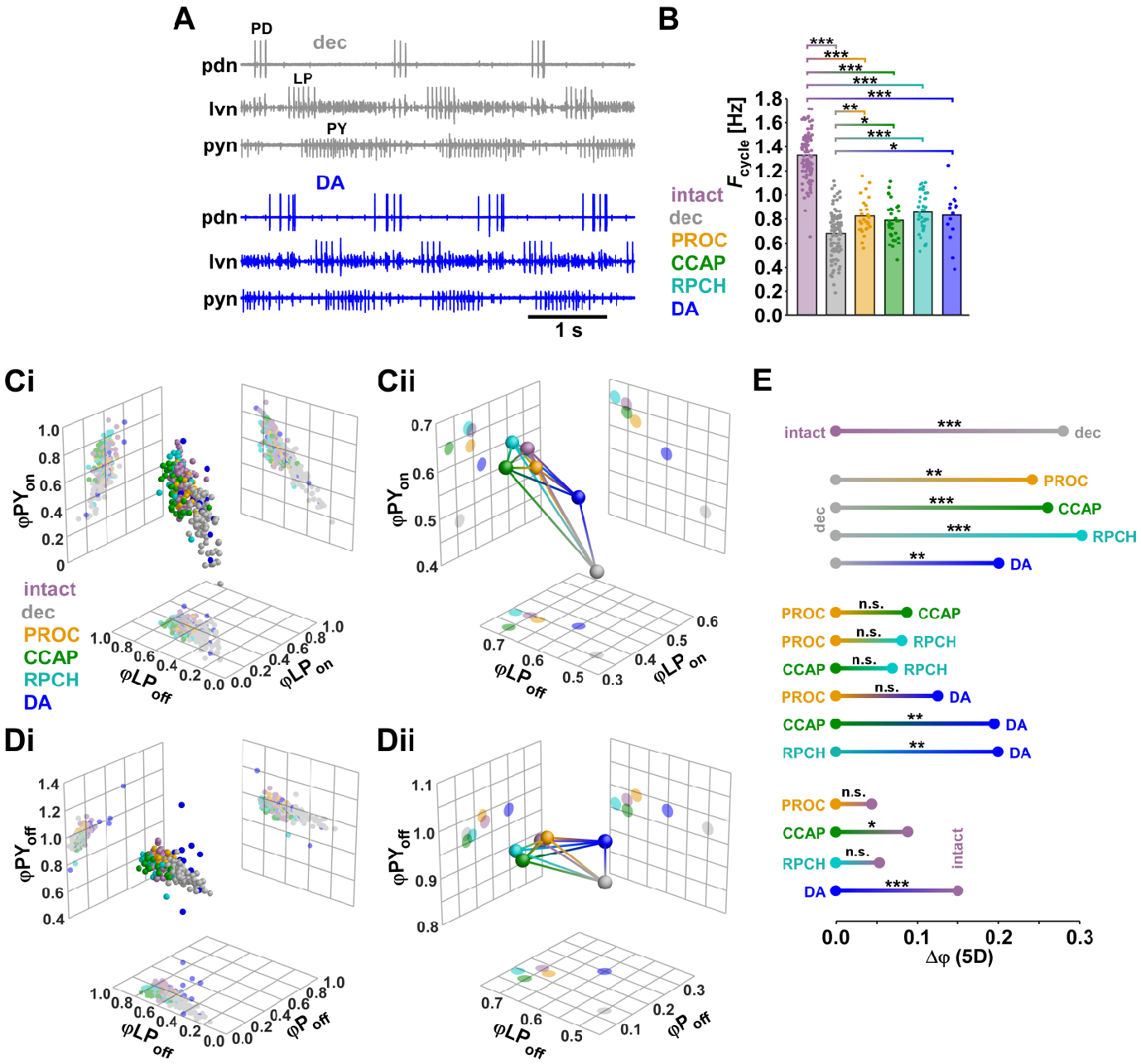
A
PD
dec
pdn
LP
lvn
PY
pyn
DA
pdn
lvn
pyn
1 s
B
intact
dec
PROC
CCAP
RPCH
DA
F_{cycle} [Hz]
Ci
Cii
Di
Dii
E
intact
dec
PROC
CCAP
RPCH
DA
n.s.
Δφ (5D)

Figure 5

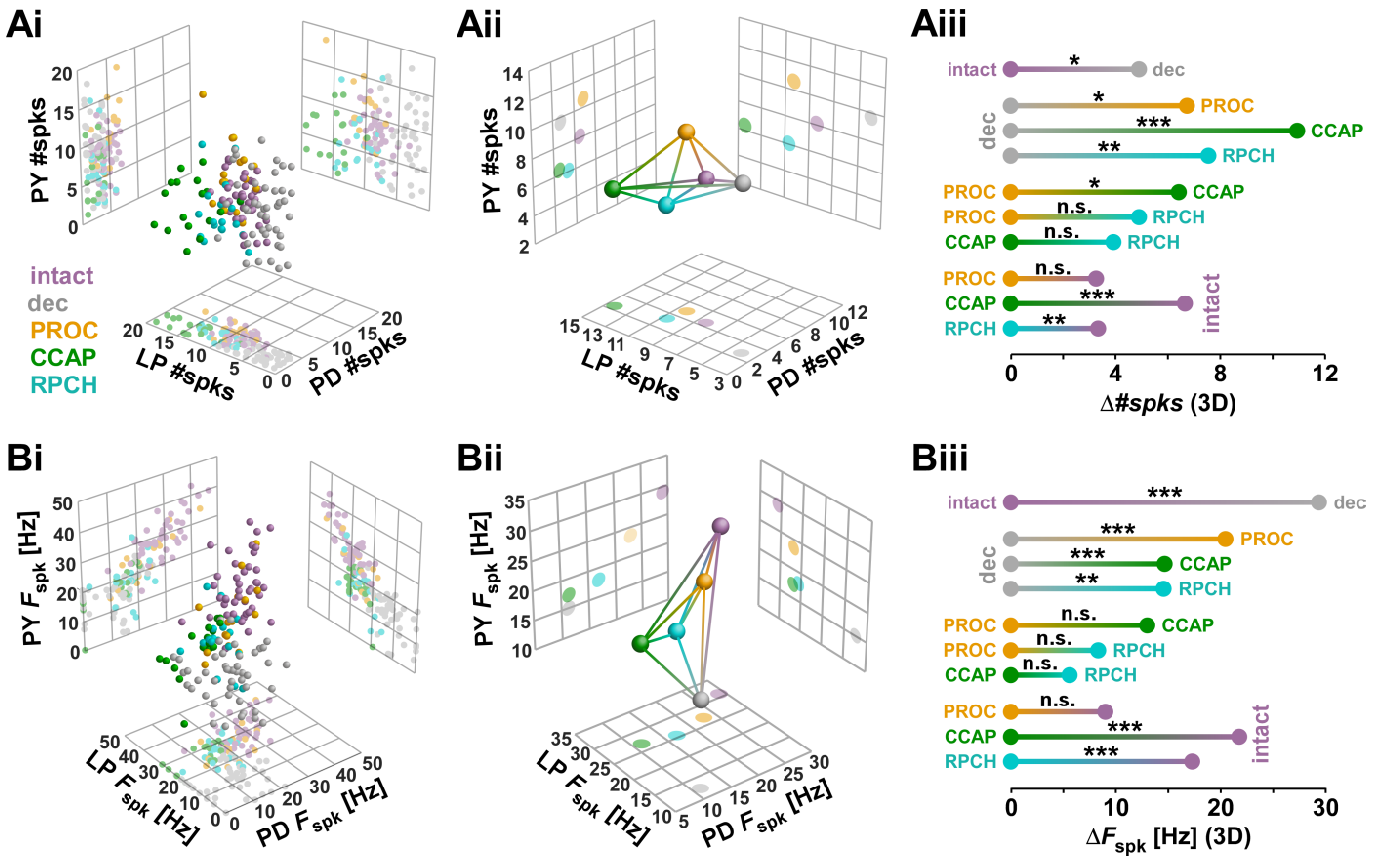
Ai
PY #spks
LP #spks
PD #spks
intact
dec
PROC
CCAP
RPCH
Aii
PY #spks
LP #spks
PD #spks
Aiii
intact
dec
PROC
CCAP
RPCH
*
***
**
n.s.
Δ#spks (3D)
Bi
PY F_{spk} [Hz]
LP F_{spk} [Hz]
PD F_{spk} [Hz]
Bii
PY F_{spk} [Hz]
LP F_{spk} [Hz]
PD F_{spk} [Hz]
Biii
intact
dec
PROC
CCAP
RPCH
***
**
n.s.
ΔF_{spk} [Hz] (3D)

Figure 6

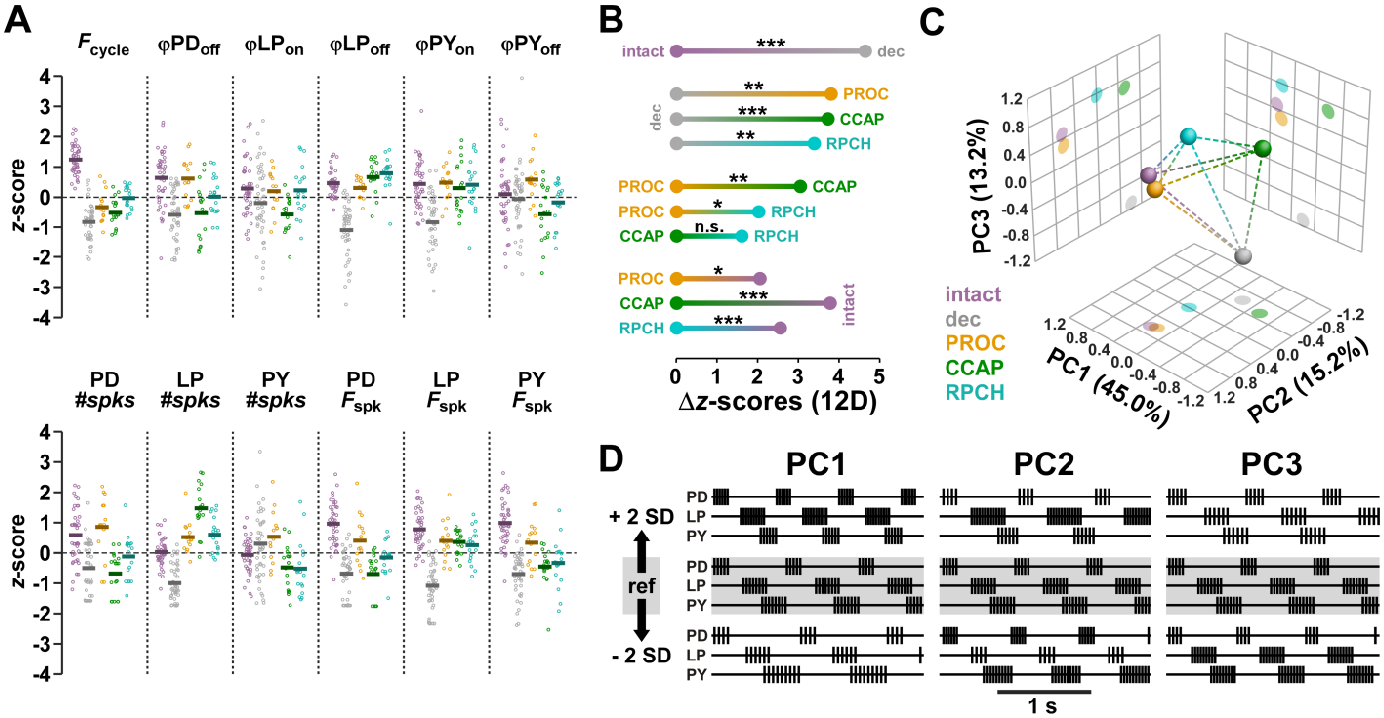
A
F_{cycle}
φPD_{off}
φLP_{on}
φLP_{off}
φPY_{on}
φPY_{off}
z-score
PD #spks
LP #spks
PY #spks
PD F_{spk}
LP F_{spk}
PY F_{spk}
B
intact
dec
PROC
CCAP
RPCH
n.s.
Δz-scores (12D)
C
PC3 (13.2%)
PC1 (45.0%)
PC2 (15.2%)
intact
dec
PROC
CCAP
RPCH
D
PC1
PC2
PC3
+ 2 SD
ref
- 2 SD
PD
LP
PY
1 s

Figure 7

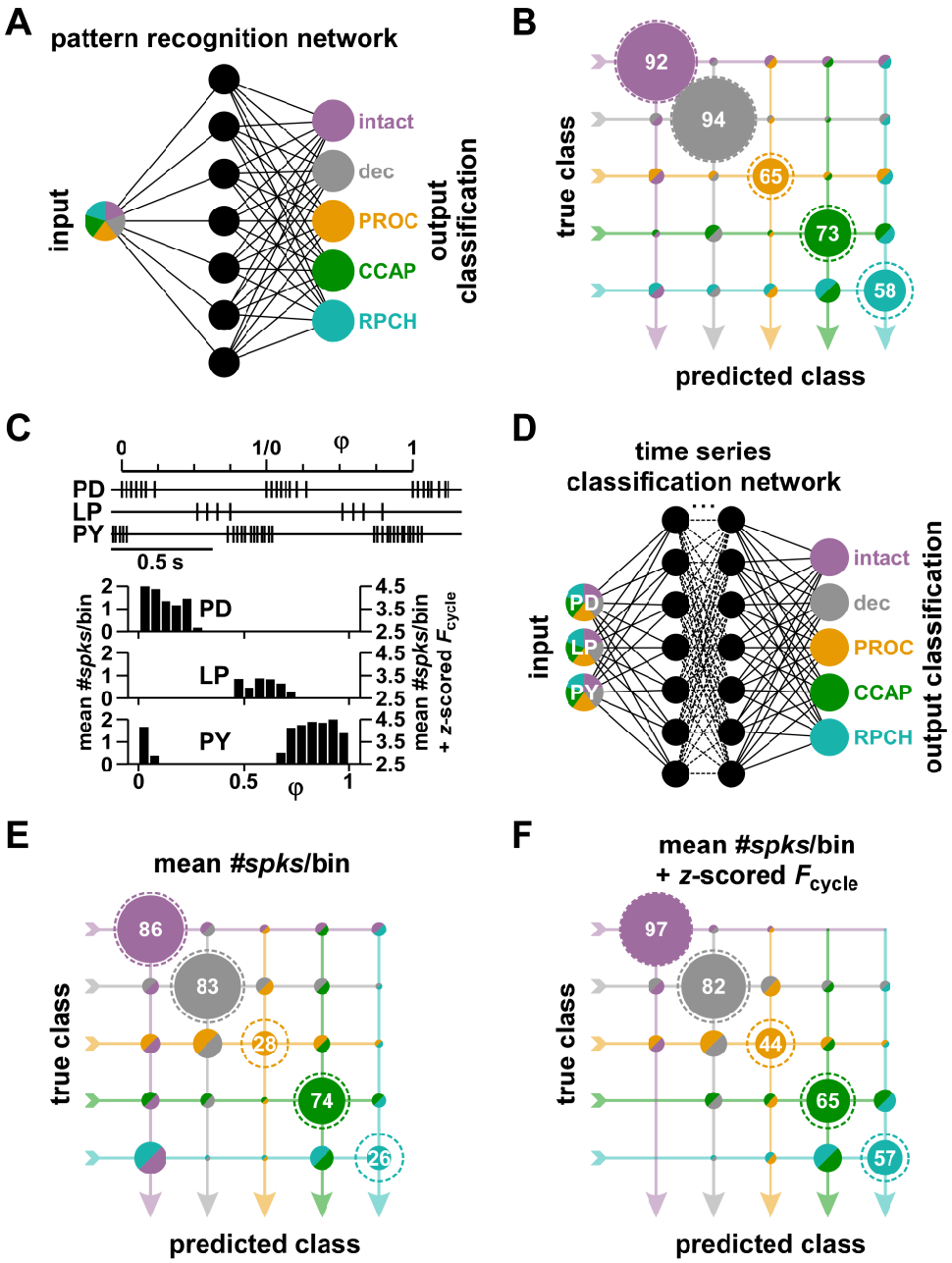
A
pattern recognition network
input
intact
dec
PROC
CCAP
RPCH
output classification
B
true class
predicted class
92
94
65
73
58
C
0
1/0
φ
1
PD
LP
PY
0.5 s
mean #spks/bin
mean #spks/bin + z-scored F_cycle
0.5
D
time series classification network
input
output classification
E
mean #spks/bin
86
83
28
74
26
F
mean #spks/bin + z-scored F_cycle
97
82
44
65
57

Figure 8